H2020 FET-Open Research and Innovation Actions Project Number 766566
Antiferromagnetic spintronics (ASPIN)

Work package 2, Deliverable D2.3: Report on software module on AF modeling for open-source multi-physics numerical simulator (OMNeS)

This report summarizes the work of the ASPIN project consortium exploring antiferromagnetic textures. We also give references to our corresponding publications containing additional information. The teams' contributions to this work were as follows:

- Institute of Physics in Prague (IOP): Materials growth and characterization, structural microscopy
- University of Nottingham (NOT): Materials growth and characterization, magnetic microscopy
- Johannes Gutenberg University in Mainz (JGU): Software development, theory

Contents

1 Overview **1**

2 Software module for antiferromagnetic modeling **2**

3 Quenched nano-fragmented domain states in CuMnAs **3**
3.1 X-ray magnetic linear dichroism photoemission electron microscopy 3
3.2 NV-diamond microscopy 4

4 Structural defects in CuMnAs **10**

5 Correlation between defects and domain structure in CuMnAs **12**

1 Overview

The current-induced writing mechanism considered in our initial concept of antiferromagnetic memory devices was based on extending the established relativistic spin-orbit torque in ferromagnets with global inversion symmetry braking to the staggered spin-orbit torque in special antiferromagnetic lattices with local symmetry breaking [1, 2, 3]. Readout was due to anisotropic magnetoresistance (AMR) which was used already in the first generation of ferromagnetic random access memories (MRAMs). The memory effect, again in analogy to ferromagnets, results from switching between ground states with different directions of the collective magnetic order vector. Consistent with this picture, X-ray magnetic linear dichroism - photoemission electron microscopy (XMLD-PEEM) showed reproducible, reversible, and stable switching of large, micron-scale antiferromagnetic domains, controlled by the polarity of the writing current of amplitude $\sim 10^6$ Acm^{-2} [4]. However, microscopies using XMLD-PEEM and scanning NV-diamond techniques have recently allowed us to identify a new pulse-induced switching mechanism to metastable nano-fragmented domain states in CuMnAs at current amplitudes $\sim 10^7$ Acm^{-2}, with the domain fragmentation reaching a 10 nm scale [5, 6]. The new switching paradigm remedies weaknesses of the first-generation devices, namely their small readout signals and the writing mechanism limited to only a special type of antiferromagnetic structures [2, 1]. (With the new switching meachnism, the readout signals reach 100% in a simple bar resistor made of a single-layer antiferromagnetic film.) Moreover, it opens possibilities with no counterparts in any of the earlier developed spintronics concepts. The prime example here is the universality of the new switching

mechanism, which is applicable from dc to fs-laser pulses and thus bridges spin electronics and ultrafast opto-spintronics by the same underlying operation principle [5]. The availability of both electrical and optical modes of switching also implies that the new concept is in principle applicable to the entire family of antiferromagnets, including metals and insulators. This significantly enlarges the materials playground for spintronics since antiferromagnets are much more abundant than ferromagnets.

A crucial information we have obtained from the swithching measurements of the quenched nano-fragmented domain states is that the heating reached during the writing pulse is in the vicinity of the antiferromagnetic transition temperature in CuMnAs ($T_N = 480$ K), in analogy to all-optical switching of ferrimagnets and ferromagnets. The memory characteristics of the nano-fragmented states is multi-level with smooth and tunable time-dependence of the relaxation of a universal Kohlrausch stretched-exponential form [5]. In contrast, devices based on switching between ground states with different directions of the collective magnetic order vector are commonly digital (bistable) and the memory loss takes a form of stochastic fluctuations between the two states. The accurate fit of our readout signals by the Kohlrausch model of relaxation in complex systems is, on one hand, fully consistent with the direct images of the complex nano-fragmented domain states observed by the magnetic microscopies. Simultaneously, the Kohlrausch relaxation is an example, noted in the past in a range of physical systems [7], that reproducible and universal behavior can transcend the details of the complex disordered materials and of the measurement probes. Indeed, we have observed high reproducibility of the above switching characteristics across different physical samples and experimental set-ups. The inferred picosecond relaxation attempt time, corresponding to the dynamics time-scales in antiferromagnets, is another key characteristics of the metastable state that we have identified. For more details on the switching characteristics see Report 1.3.

In complementary structural characterizations [8] we have shown that our single-crystal CuMnAs layers grown by molecular beam epitaxy with the best substrate matching, stoichiometry, uniformity, and minimized abundance of defects have optimized characteristics of the resistive switching signals corresponding to the quenched metastable nano-fragmented domain states. Also, X-ray absorption PEEM, X-ray diffraction, scanning electron microscopy, and transmission electron microscopy measurements have confirmed no signs of electromigration or structural transitions of the CuMnAs epilayers for currents and heating conditions corresponding to the switching experiments [8, 5]. While no correlations to structural defects have been identified for the quenched metastable nano-fragmented domain states, XMLD-PEEM measurements revealed a strong correlation between the defect structure and the equilibrium domain structure in antiferromagnetic CuMnAs. The micromagnetics and switching dynamics are, therefore, much richer in antiferromagnets than originally anticipated when considering the initial concept of Néel vector reorientation by spin-torques. In our original development plan for the software module on antiferromagnetic modelling we were not aware of this intriguing complexity of antiferromagnets. Therefore, after the initial development steps (see examples below), we paused further work on the modelling software until these new observations have been experimentally firmly established and analyzed. This is way the main part of this report focuses on the experimental magnetic and structural microscopy studies [5, 6, 8].

2 Software module for antiferromagnetic modeling

The software module OMNeS is based on high performance, easy to customize, multi-physics solvers able to handle the complex interplay between new physics at the nano-scale and the non-trivial geometry of real life devices and experiments. A key feature of OMNeS is scalability, meaning the ability to scale cost-effectively to very large size simulations. This is being enabled by leveraging on well-established software technologies and being pre-packaged for easy deployment to cloud computing infrastructures. In Figs. 1 we illustrate that OMNeS uses unstructured grids (meshes) suitable for realistic device or microstructure modelling. In Figs. 2-4 we show examples of the initial simulations obtained by the antiferromagnetic module of OMNeS: The stabilization of an isolated skyrmion texture by exchange, anisotropy and Dzyaloshinskii-Moriya (DMI) interaction for an ultra-thin film

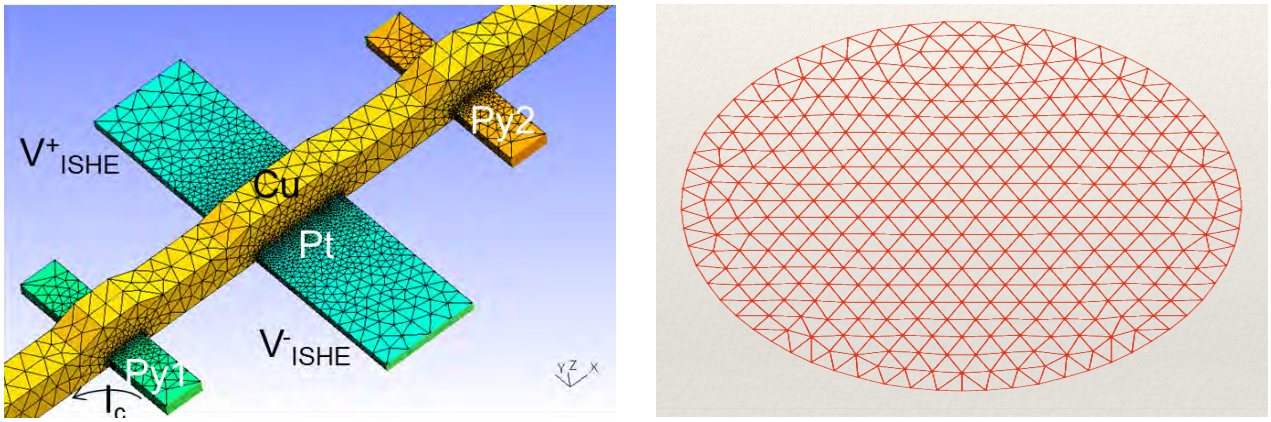

Figure 1: OMNeS uses unstructured grids (meshes), realistic device or microstructure modelling.

antiferromagnetic nano-disk, an example of non-zero oscillating net magnetization in an antiferromagnetic skyrmion, gyrotropic dynamics mode, and traveling antiferromagnetic spin-wave mode confined at the disk edge.

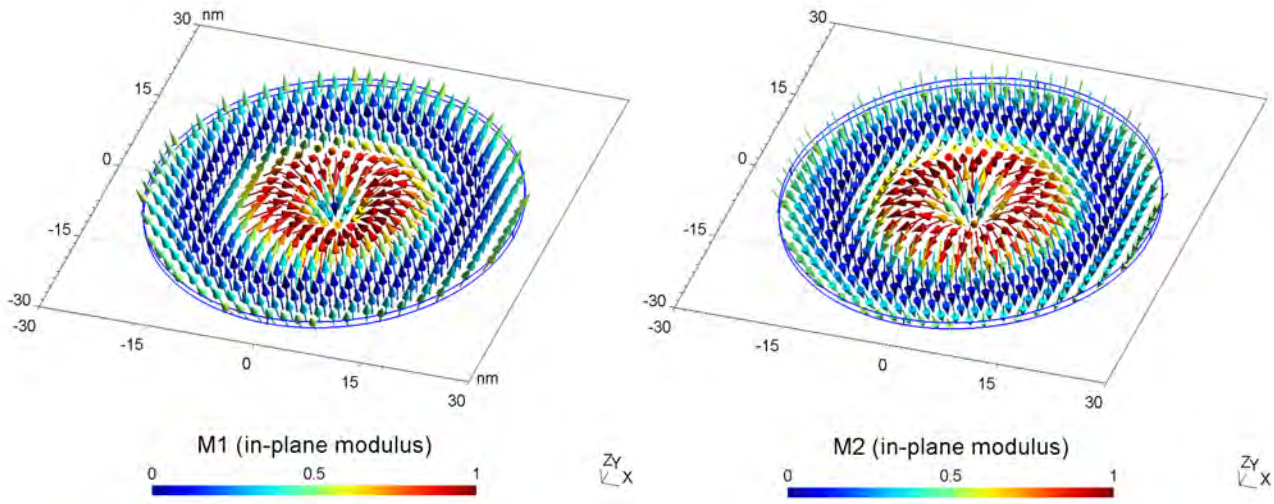

Figure 2: For an ultra-thin film AFM nano-disk, exchange, anisotropy and DMI stabilize an isolated skyrmion texture.

3 Quenched nano-fragmented domain states in CuMnAs

3.1 X-ray magnetic linear dichroism photoemission electron microscopy

Switching of the Néel vector controlled by the direction of current pulses in CuMnAs devices was studied in detail by XMLD-PEEM [4]. Here the images showed reproducible, reversible, and stable switching of large, micron-scale antiferromagnetic domains. These microscopy images were found consistent with the expected symmetry of the staggered current-induced field and correlated with the measured fraction of a per cent AMR. The threshold pulse currents for observing the switching were around 10^6 Acm^{-2} and the currents were kept below 10^7 Acm^{-2}, preserving the large domain state of the pristine film [4]. The small AMR amplitude was independently confirmed in our recent study where the Néel vector reorientation in CuMnAs was induced by a strong external magnetic field [9].

The new switching mechanism into nano-fragmented domain states is observed at writing currents above 10^7 Acm^{-2} [5]. The resulting readout signals exceed the earlier observed signals due to AMR

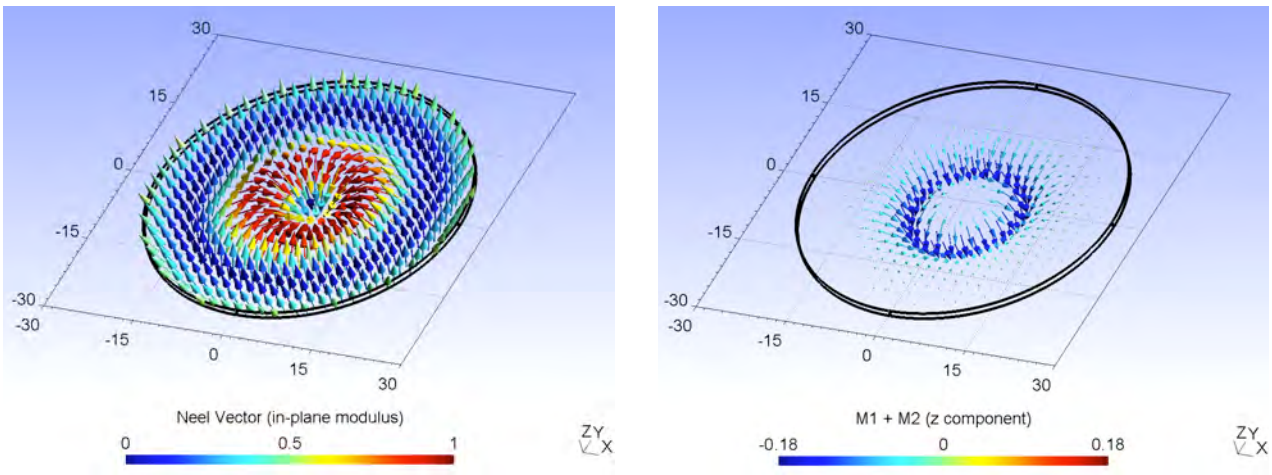

Figure 3: An example of non-zero, oscillating net magnetization of an antiferromagnetic skyrmion.

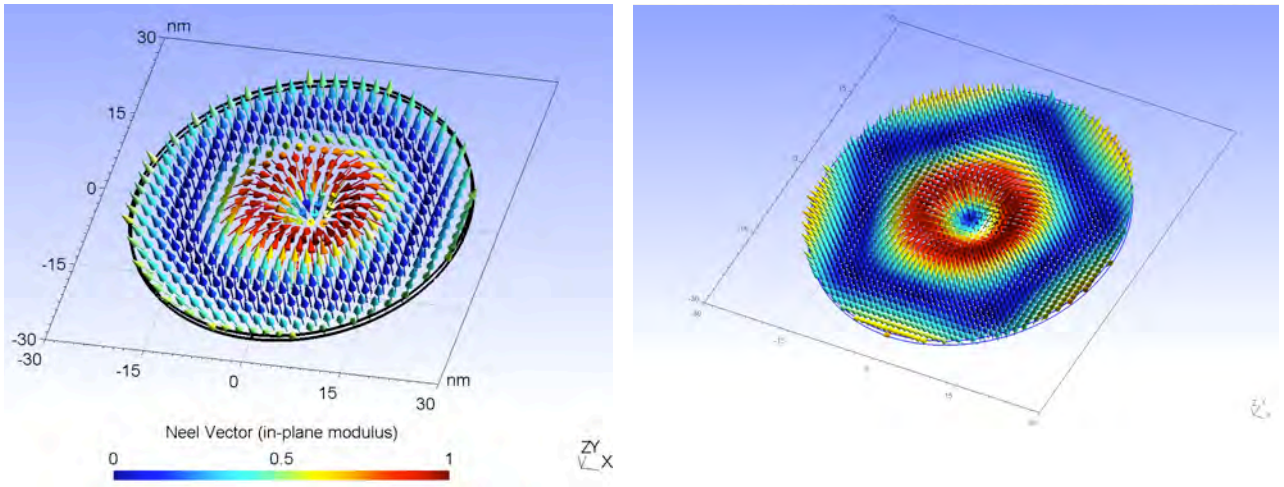

Figure 4: Left: two degenerated (cw/ccw) gyrotropic mode; right: traveling antiferromagnetic spin-wave mode confined at the disk edge.

by up to three orders of magnitude. The mechanism allows us to downscale writing to a single fs-laser pulse and an unprecedented control of device characteristics. The pulse-induced fragmentation of antiferromagnetic domains observed by the XMLD-PEEM measurements is presented in Fig. 5. The PEEM images were obtained on beamline I06 at Diamond Light Source, using an Elmitec SPELEEM-III microscope to image secondary-electron emission arising from X-rays incident on the sample at a grazing angle of 16°. The probe depth was $\approx$ 7 nm, and the lateral resolution was $\approx$ 50 nm. A pulsing power supply was connected to the sample in ultrahigh vacuum via feedthroughs to the sample holder. Magnetic contrast images were obtained using the XMLD asymmetry, which measures the local surface Néel vector. We acquired images for each X-ray energy during 1s exposure times, and we averaged 20 images to obtain a single XMLD-PEEM image. For more details see Ref. [4].

3.2 NV-diamond microscopy

In a complementary laboratory microscopy, we investigated [6] the antiferromagnetic domain pattern of the CuMnAs films by recording their nanoscale magnetic stray field using scanning NV magnetometry [10, 11]. This is a powerful microscopy technique for investigating weak magnetic patterns with high spatial resolution, with applications to nanometer-scale magnetism. In the following, we demonstrate that scanning NV magnetometry is capable of imaging the magnetic state of in-plane antiferromagnets

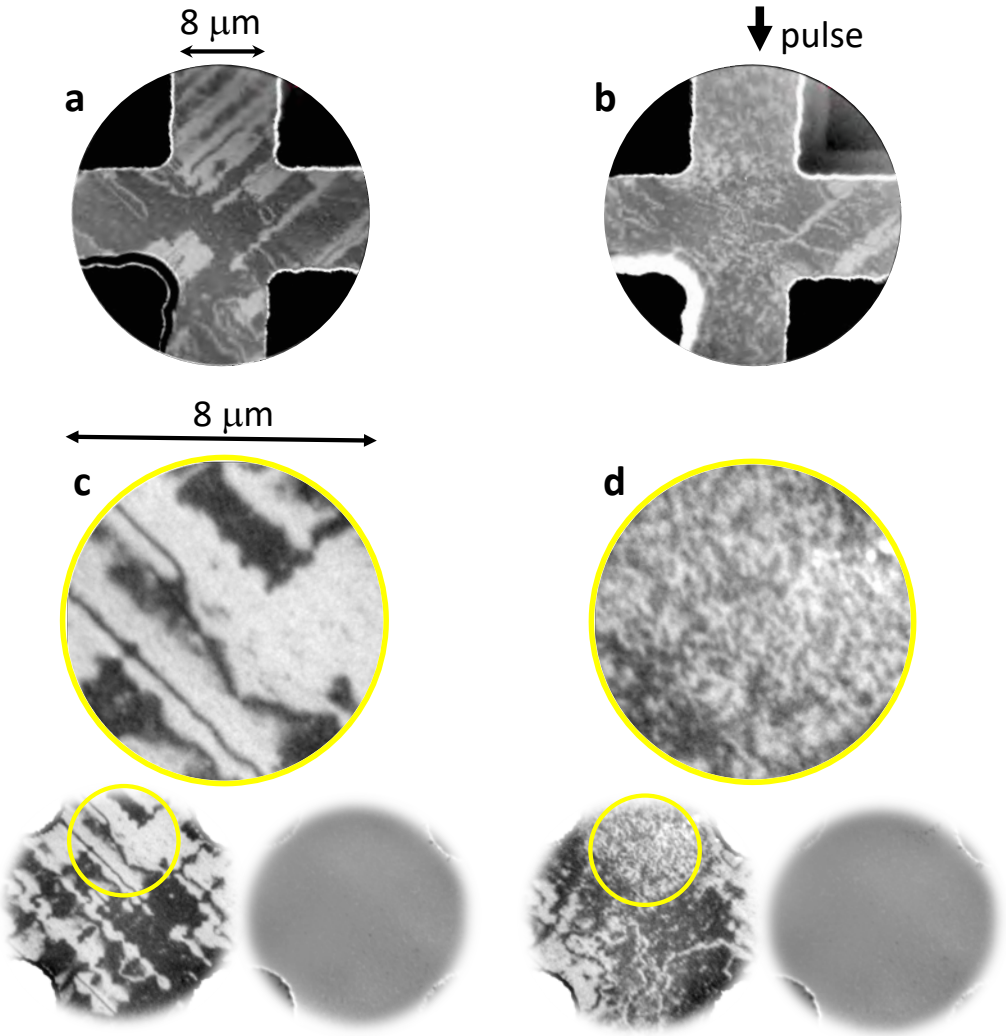

Figure 5: **a,** Antiferromagnetic domain structure of an as-fabricated CuMnAs(50nm)/GaP sample observed by XMLD-PEEM for X-ray polarization $E \parallel [1\bar{1}0]$ crystal axis. The light (dark) contrast corresponds to antiferromagnetic domains with the Néel vector oriented parallel (perpendicular) to the X-ray polarization. **b,** Same as **a**, after applying a 500 μs current pulse of amplitude $\approx 1 \times 10^7$ Acm^{-2} along the vertical ([010]-oriented) direction (black arrow). **c,** Bottom-left and top zoomed-in: XMLD-PEEM image of the antiferromagnetic domain structure of an as-fabricated CuMnAs(45nm)/GaP sample. Bottom right: X-ray absorption PEEM without XMLD contrast. **d,** Same as **c**, after applying a 100 ms current pulse of amplitude $\approx 1 \times 10^7$ Acm^{-2} along the vertical ([010]-oriented) direction. For more details see Refs. [4, 5].

and we develop a model that relates the magnetic stray field to the structure of the antiferromagnetic domains.

Our samples are 30-nm- and 50-nm-thick CuMnAs films grown by molecular beam epitaxy on a GaP (001) substrate. Tetragonal CuMnAs films consist of alternating layers with opposite in-plane magnetization. The crystal and magnetic structure of CuMnAs are shown in Fig. 6a. The possible set of domain orientations in these samples is restricted by the magnetic anisotropy: in thinner films ($t < 50\,$nm), the anisotropy tends to be uniaxial with a 180° reorientation of the Néel vector between adjacent domains. Thicker films have a stronger biaxial component and both 90° and 180° domain walls are present [4, 12]. XMLD-PEEM images indicate Néel-type domain walls with the Néel vector rotating in the $a - b$ plane [4].

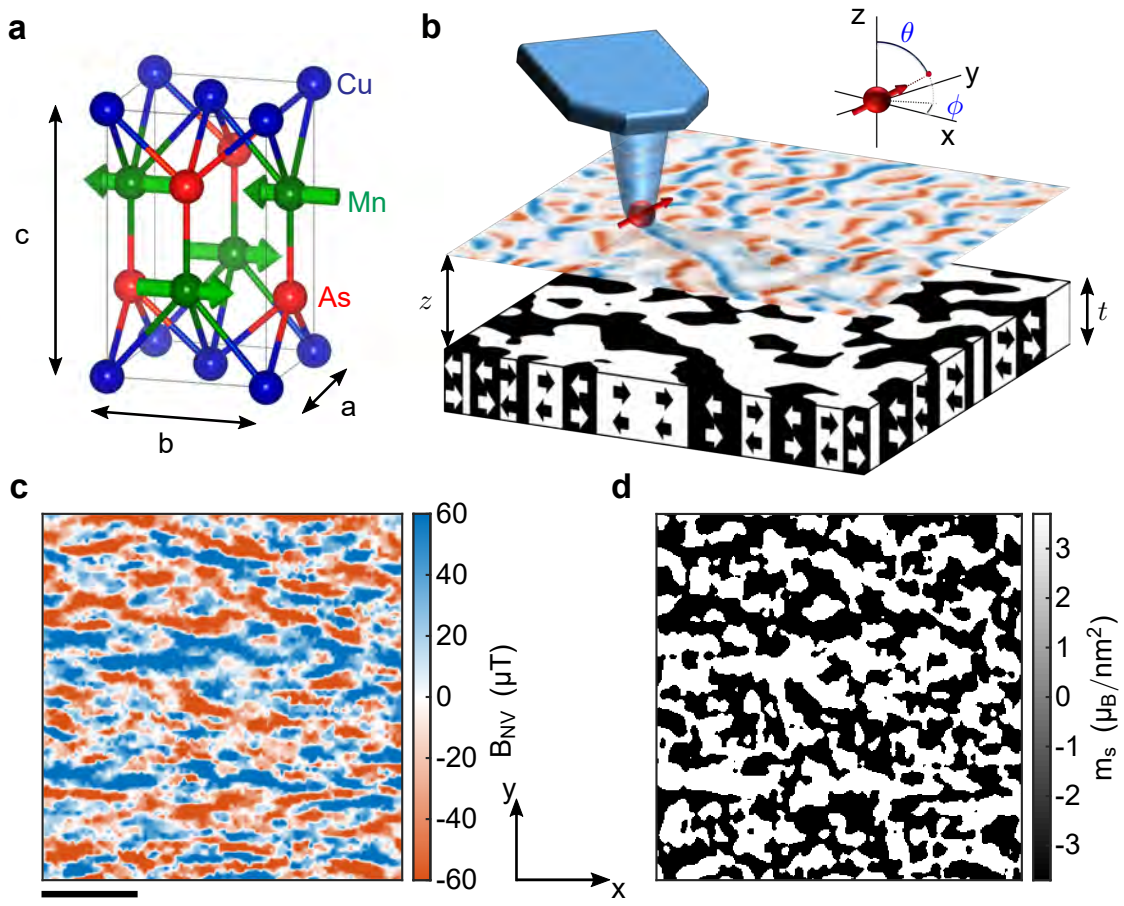

Figure 6: **Scanning NV magnetometry on CuMnAs. a,** Unit cell of CuMnAs. The magnetic moments of the Mn^{2+} ions (green arrows) are oriented in plane and alternate along the [001] direction (the c-axis). **b,** Schematic of the scanning NV magnetometer. A diamond tip (blue) containing an NV centre (red arrow) is scanned over an antiferromagnetic film (thickness $t = 30 - 50\,\mathrm{nm}$). Antiferromagnetic domains are represented by black and white areas with co-planar spins. The scanning NV magnetometer records the antiferromagnet's magnetic stray field $B_{\mathrm{NV}}(x, y)$ at a distance $z = 50 - 100\,\mathrm{nm}$ above the surface (red/blue pattern). The inset defines the (θ,ϕ) vector orientation of the NV centre. **c,** Example of a magnetic stray field map of a pristine 30-nm-thick CuMnAs film. NV centre parameters are ($z = 60 \pm 7$ nm, $\phi = 270° \pm 5°$, $\theta = 55°$). **d,** Domain pattern reconstructed from the field map in panel c, as described in the text. Scale bar, 800 nm.

Figure 6b depicts a schematic of the measurement principle. A diamond probe containing a single NV centre at the apex is scanned at constant height ($z \sim 50 - 100\,\mathrm{nm}$) above the sample surface. At every location we measure the shift in the NV centre's spin resonance using optical readout [11], which is directly proportional to the magnetic stray field $B_{\mathrm{NV}}(x, y)$ at that location. Note that the NV centre is sensitive only to the field component parallel to its symmetry axis, which lies at an angle $\theta = 55°$ off the surface normal for our probes (see inset to Fig. 6b). Using the known vector orientation of the NV center, the full magnetic vector field at the NV centre position can be reconstructed. Figure 6c shows an example magnetic stray field map recorded from a 30 nm-thick CuMnAs film.

The reconstructed domain pattern from Fig. 6c is shown in Fig. 6d. We find that the easy axis is approximately pointing along the [110] ($\pm y$) direction. Note that the magnetic field map in Fig. 6c reflects the morphology of the domain pattern shown in Fig. 6d, provided that the spatial sensitivity is comparable to the feature size. Comparison with XMLD-PEEM images [13, 4] reveals similar domain patterns as those observed in Fig. 6d.

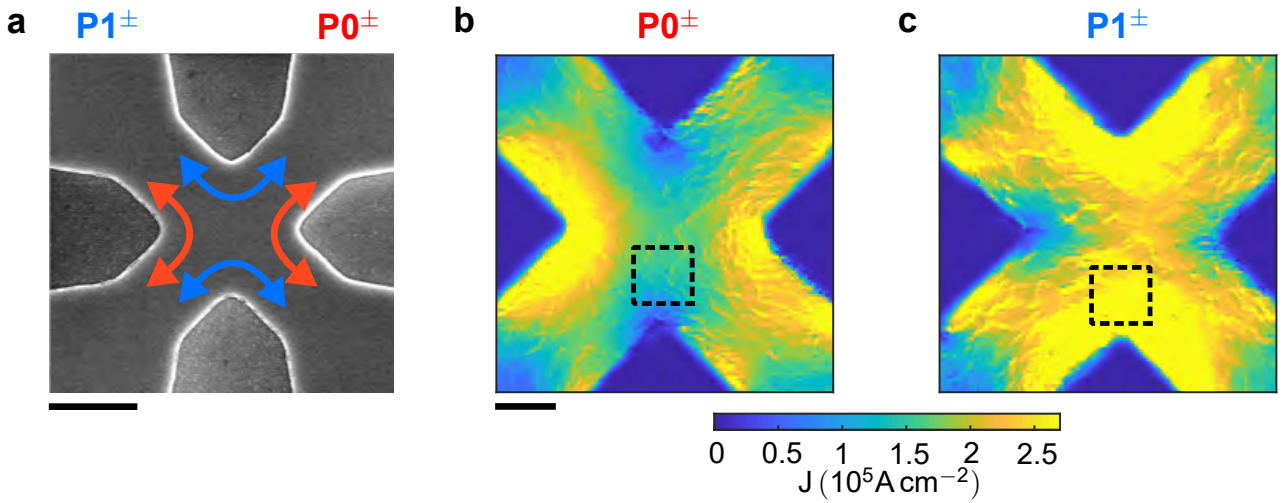

Figure 7: **Current distribution, electrical resistance, and magnetic stray field maps of the relaxed state after switching. a,** Scanning electron micrograph of a representative cross-shaped CuMnAs device. The arms of the cross are 5-μm-wide and oriented parallel to the [100] and [010] crystal axes of the CuMnAs film. The pulse directions are defined as $P0^{\pm}$ (red arrows) and $P1^{\pm}$ (blue arrows). The sign denotes polarity. Scale bar, 5 μm. **b,c,** Current density distribution for $P1$ and $P0$ pulses measured using scanning NV magnetometry for a probe current of 1 mA. Scale bar, 2 μm.

Figure 7 shows the cross-shaped geometry of a patterned CuMnAs device used for electrical pulsing experiments. We define the orthogonal current directions $P0^{\pm}$ and $P1^{\pm}$ in Fig. 7a, where $\pm$ indicates the polarity of the pulse. In a first step, we image the current density distribution by recording the Oersted field. In Fig. 7b we show the current distribution for the current direction $P0^{\pm}$. The current density is highest at the corners of the cross, as expected, and presents a granular texture that changes from device to device. Figure 2c shows an analogous current density map recorded for $P1^{\pm}$.

To probe the domain structure during the initial fast decay of the electrical resistance, corresponding to the grey shaded region in Fig. 8a, we implement a pump-probe scheme that interleaves the data acquisition with electrical current pulsing. We also vary the current density to probe the relaxation after pulses that induce changes of R_{xy} in the mΩ to Ω range, as shown in Fig. 8b. In the pump-probe method, described in Fig. 8c, we apply a writing current pulse before the acquisition of each pixel and measure B_{NV} during the first 4 s right after the pulse. Two scans are recorded at the same time, with their pixels interleaved, one after application of a $P0^{+}$ pulse, the other after a $P1^{+}$ pulse. In this way we are able to probe the magnetic state averaged over the first 4 s of the relaxation process for both current directions. For these measurements we probe the central region of the cross shaped devices, where approximately the same current density can be expected for $P0$ and $P1$ pulses. Examples of stray field images acquired in the pump-probe mode for a 30 nm thick CuMnAs film are shown in Figs. 8d-g.

We first focus on writing currents close to the density threshold of the large switching R_{xy} signal. In Fig. 8a we show the time-dependence of R_{xy} after a 100 μs writing pulse of average current density $J = 1.89 \times 10^7$ A cm^{-2}, which is just above the threshold shown in Fig. 8b. The first image (Fig. 8d) acquired after $P0^{+}$ pulses with $J = 1.89 \times 10^7$ A cm^{-2} shows a stray field pattern very similar to that of the pristine sample, indicating that the current density in the centre of the cross is not sufficient to modify the antiferromagnetic domains in an appreciable way. Upon increasing the current density to $J = 1.98 \times 10^7$ A cm^{-2}, however, we observe a striking reduction of the amplitude of the magnetic stray field (Fig. 8f), which we quantify by taking the root mean square of $B_{NV}(x, y)$ over the entire magnetic field map, B_{rms}, see methods. The reduction in B_{rms} is similar for the images acquired after $P0^{+}$ and $P1^{+}$ pulses (Fig. 8e,f), indicating that the direction of the writing current does not play a role in this effect.

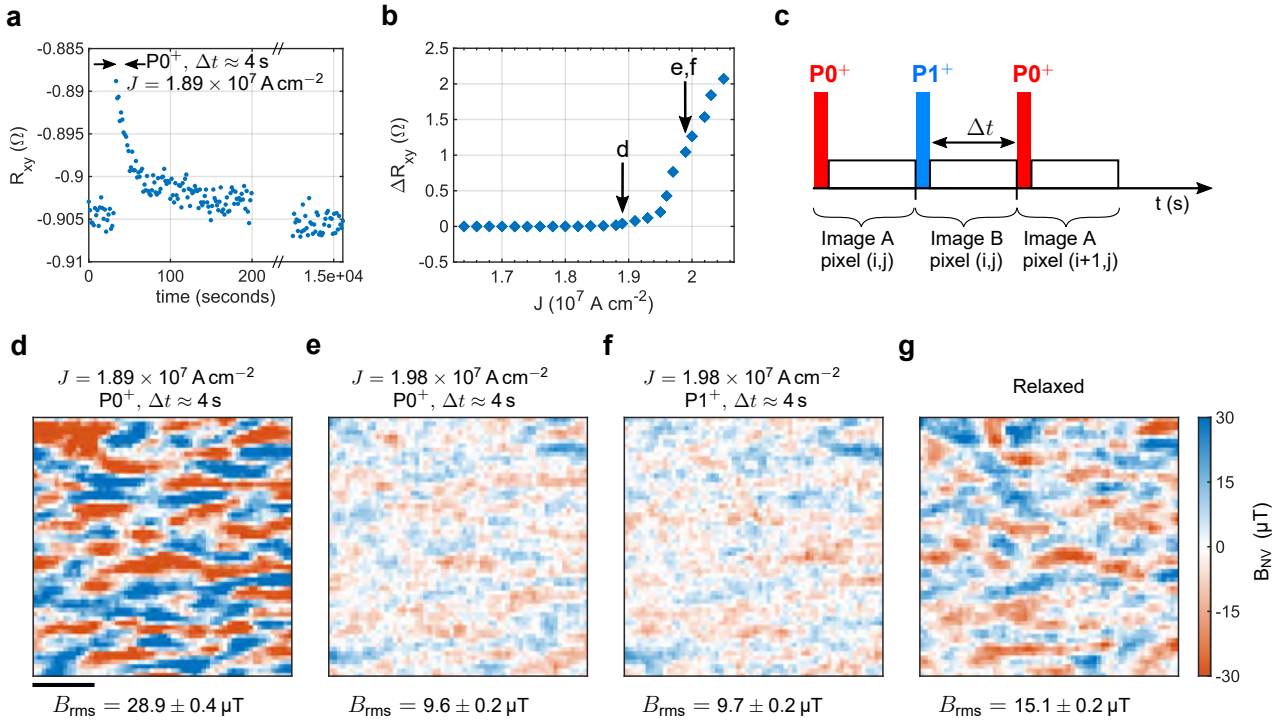

Figure 8: **Pump-probe measurement scheme and stray field maps of the excited and relaxed states.** **a,** Temporal evolution of R_{xy} after application of a single $P1^+$ current pulse of amplitude $J = 1.89 \times 10^7$ A cm^{-2} and duration 100 μs to a 30 nm thick CuMnAs device. **b,** Current density J vs. maximum switching amplitude R_{xy}. **c,** Schematic of the measurement sequence. For each image pixel (i, j) we measure the magnetic stray field twice, once after a $P0^+$ pulse and once after a $P1^+$ pulse. The stray field measurement starts immediately after a pulse and is integrated over $\Delta t = 4$ s (grey shaded area region in panel a). This sequence is repeated pixel by pixel to build up the images shown in panels d-g. **d-g,** Magnetic stray field maps of the 30 nm thick CuMnAs film after $P0^+$ pulses (d,e), $P1^+$ pulses (f), and 75 hours after the last pulse (g). The measurements are performed in the centre of the cross and the pulse amplitude is given above each scan. The sensor parameters are ($z \approx 52 \pm 11$ nm, $\phi \approx 88° \pm 5°$, $\theta \approx 55°$). Scale bar, 400 nm.

Once the pulsing stops, the stray field amplitude slowly recover on a time scale of days. The relaxed image (Fig. 8g), which is acquired 75 h after applying the last pulse from Fig. 8f, shows that the system maintains a memory of the pristine domain configuration even after a long sequence of excitations. The memory effect is not perfect, as can be seen by comparing the upper left corner of Fig. 8d-g, but pervasive to both the excited and relaxed states.

We now argue that the reduction of the stray field amplitude is caused by a decrease of the average domain size. This behavior can be understood by simulating the stray field produced by varying domain configurations. Starting from a model of the pristine domain configuration and its stray field pattern, shown in Figs. 9a and 9b, respectively, we generate a magnetization pattern with a fragmented structure, retaining the overall shape of the domain pattern as defined by regions with a prevailing orientation of the Néel vector (Figs. 9c,d). The simulated stray field maps of the pristine and fragmented domains present a similar morphology but a different magnetic contrast, in agreement with the experiment. Alternative explanations to the reduction in magnetic contrast, such as heat-induced suppression of the magnetization m_s or a change in sensor stand-off distance z can be safely excluded, as the relaxation occurs on a much longer time scale compared to thermal effects and no drifts in the scanning setup are observed.

The decrease of B_{rms} can be qualitatively understood by noting that B_{NV} at a height z above

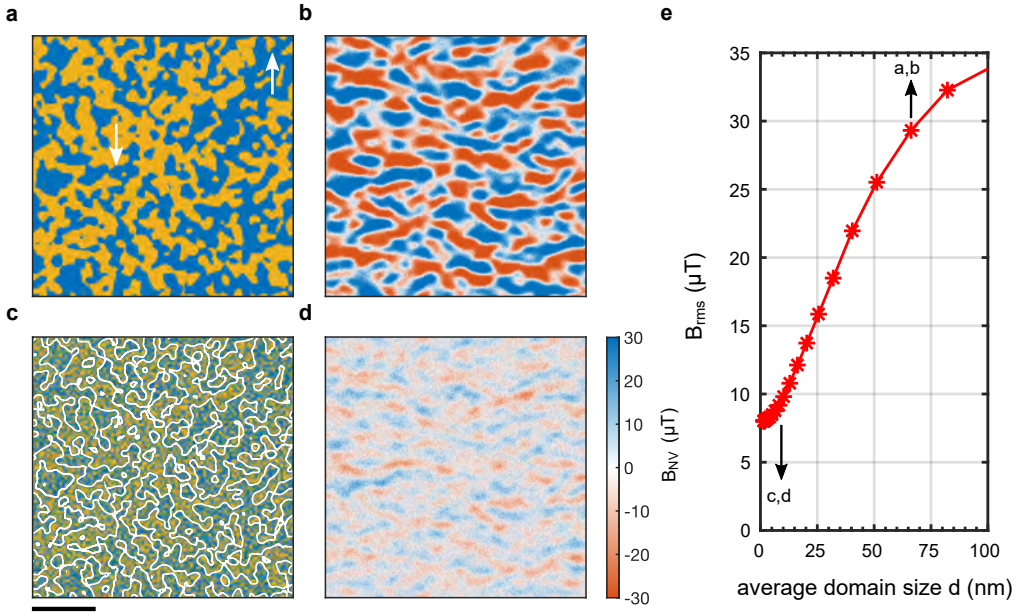

Figure 9: **Simulations of the stray field produced by a pristine and a fragmented domain pattern. a,b**, Simulated pristine domain configuration (panel a) and magnetic stray field (panel b) for a 30-nm-thick CuMnAs film. Arrows indicate the direction of the Néel vector. **c,d**, Simulated fragmented domain configuration (panel c) and magnetic stray field (panel d). White contour lines mark the pristine domain walls from panel a. The fragmentation leads to a reduction of the magnetic contrast B_{rms}, whereas the overall shape of the stray field pattern is partially conserved. Scale bar, 400 nm. **e,** Simulated B_{rms} as a function of average domain size d defined as (number of domain walls per unit length)$^{-1}$. For small domains $d < z$, the stray field is approximately proportional to d. Black arrows indicate the approximate d for the patterns plotted in panels a-d. Simulations use the same NV centre parameters as in Fig. 8.

the surface is most affected by changes of the magnetization that occur on the same length scale as z. Much larger and homogeneous structures generate stray fields only in the vicinity of the domain walls, whereas stray field lines of more localized structures are confined to the close proximity of the surface. In the context of domain imaging, this means that finely broken-up domains are too small to be resolved by the NV sensor. Comparing the reduction in B_{rms} to the results of our numerical simulations (Fig. 9e), we estimate that the current pulsing leads to the formation of fragmented domains with a typical length scale of about 10 nm.

To gain further insight into the relationship between magnetic domains and electrical resistance, we performed a series of pump probe measurements for only one current polarity as a function of pulse amplitude. Figure 10a plots the transverse resistance R_{xy} as a function of time of a 50-nm-thick CuMnAs device while the current density is stepped up from 1.36 to 1.54 Acm^{-2}. The measurements are performed in the lower corner of the cross, where the impact of the current is highest (see Fig. 7). At each current density step, we record a stray field map using the pump-probe scheme of Fig. 8 and compute B_{rms}. As expected, the resistance signal increases with increasing current density. In addition, we observe that repeated pulsing at one set value of J leads to a further gradual increase of R_{xy}. Figure 10b shows that the increase in resistance is accompanied by a similar reduction in B_{rms}, clearly showing the correlation between the two effects. The correlation persists after the pulsing stops and the system slowly evolves towards the relaxed state (hours 38-60).

This series of measurements demonstrates that the reduction in B_{rms} does not depend on either the direction or polarity of the current, since it occurs for both orthogonal (Fig. 8) and unidirectional pulses (Fig. 10). Further experiments involving bipolar pulses show that the fragmentation occurs

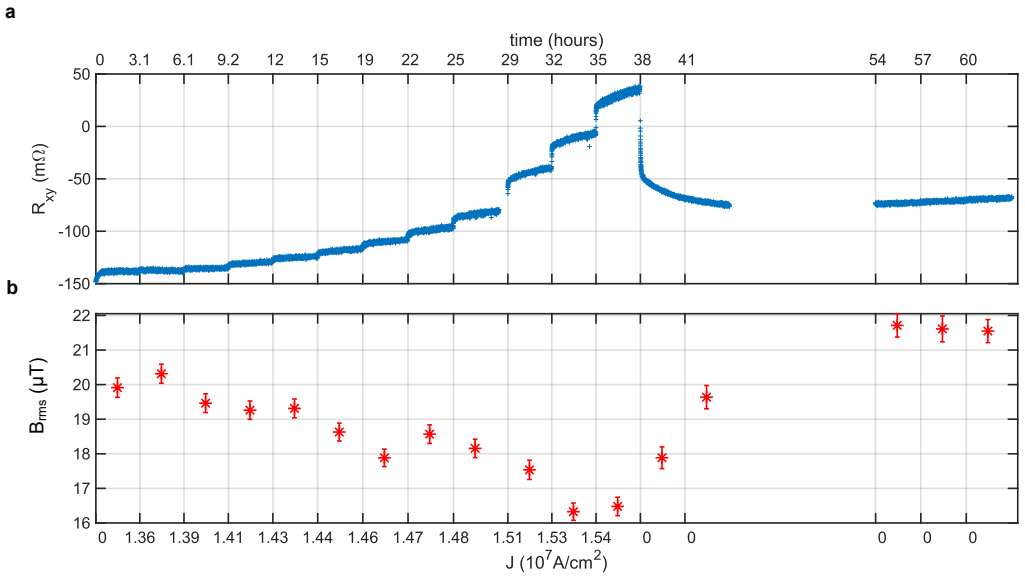

Figure 10: **Correlation between fragmentation and electrical resistance. a,** Change of the transverse resistance R_{xy} and **b,** Stray field amplitude B_{rms} versus current density J (bottom axis) and time (top axis) of the 50 nm-thick CuMnAs film. R_{xy} is plotted for every pixel in chronological order. B_{rms} is computed from stray field scans recorded at each J value in 3-hour intervals (vertical lines). The measurements are performed using the same pump-probe scheme as in Fig. 8a, but only $P1^+$ pulses are applied. The scan area is the same as in Fig. 7b,c. The NV sensor parameters are ($z = 97 \pm 2$ nm, $\phi = 96° \pm 3°$, $\theta = 55°$).

in combination with domain switching, as fragmented and relaxed images also show evidence of 180° reorientation of the Néel vector in certain areas of the scans.

4 Structural defects in CuMnAs

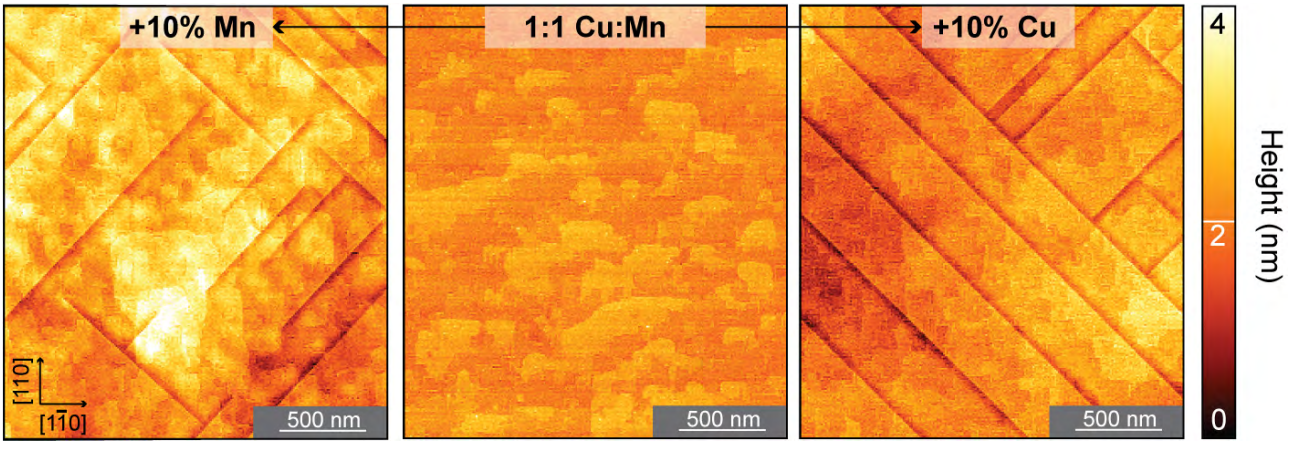

Figure 11: AFM micrograph of the surface of 50 nm thick Mn-rich, 1:1 stoichiometric, and Cu-rich CuMnAs samples grown on GaP. The highlighted crystallographic directions correspond to the orientation of the substrate.

We now review our structural microscopies of defects in CuMnAs [8]. A general trend in the surface morphology of CuMnAs epilayers as a function of the Cu:Mn flux ratio is shown in Fig. 11. While the

1:1 Cu:Mn sample has a flat surface with terraces of the unit-cell step height, the off-stoichiometric samples exhibit characteristic line-shaped surface defects oriented along the [110] and [$\bar{1}$10] directions of CuMnAs. As shown in Fig. 11, the density of these defects and so the RMS roughness steeply increase with the deviation from the 1:1 stoichiometry point.

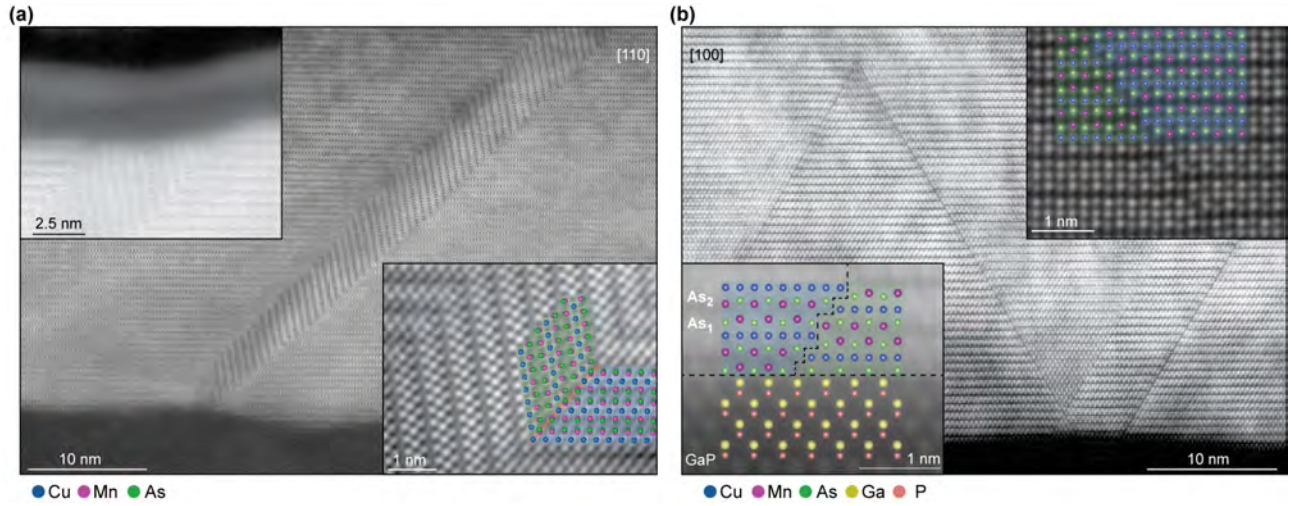

Figure 12: (a) HAADF-STEM micrograph of a twin-like structural defect propagating throughout 50 nm thick layer of CuMnAs and viewed from [110] CuMnAs (i.e. [100] GaP) direction. The lower inset shows a zoom in on the atomic structure of the defect, overalied with expected positions of Cu - blue, Mn - purple and As - green. The uper inset then shows the detail of the top interface with the Al cap. (b) HAADF-STEM micrograph of a slip dislocations presents the same 50 nm thick layer of CuMnAs, but viewed from [100] CuMnAs (i.e. [110] GaP) direction. The lower inset shows an atomic model overlay at the interface with the substrate (Ga - yellow, P - orange), where the first layer from the GaP substrate starts with either Mn/As layer As_1 or As_2. The upper inset shows zoom in on the atomic structure of one of the defects, with the atomic model overlay representing the expected structure.

The defects are not related just to the surface of the layers, but they protrude through the bulk. We have prepared thin lamelae from various 50 nm thick CuMnAs samples by focused ion beam (FIB) technique in order to study the atomic structure of the defects. The high-angle annular dark field - scanning transmission electron microscopy (HAADF-STEM) analysis revealed two characteristic types of defects which were present in all studied samples. The first type is visible in the [110] projection of CuMnAs, as shown in Fig. 12(a). It is of the micro-twin type and consists of a thin slab of CuMnAs crystal lattice rotated by 81.9 deg, which corresponds to the angle between (111) and ($\bar{1}\bar{1}$1) planes. The slab propagates through the whole thickness of the 50 nm CuMnAs film, mostly following the same (111) or ($\bar{1}\bar{1}$1) planes. At the surface the micro-twin slabs project as characteristic defect lines along [100] and [010] directions of CuMnAs, as shown in Fig. 11. Based on the depth profile measured across the surface defect lines by AFM, it is possible to determine the sign of the tilt of the corresponding micro-twin beneath (see the upper inset in Fig. 12(a)). The typical width of the micro-twins is several nanometers. The STEM images show that there is a significant amount of strain in the CuMnAs crystal surrounding the micro-twins. Therefore, the micro-twin density is directly correlated to the amount of strain in the CuMnAs crystal. Finally, it should be noted that after investigating multiple different samples, we have not found any consistent correlation between the micro-twin defect location and the local morphology of the underlying substrate (presence of surface steps, misfit dislocations, or other types of defects). The only direct correlation we have found is that the defect density increases with the deviation from the 1:1 stoichiometry point.

The second type of the characteristic defects can be seen on lamelae cut along the (100) planes of CuMnAs. Their typical structure is shown in Fig. 12(b). The apparent c/2 slip dislocations form

anti-phase boundaries along the (011) or (0$\bar{1}$1) planes and always start at the substrate-film interface, similarly to the micro-twin defects. They can either protrude throughout the whole thickness of the film, or annihilate in a finite depth when two such defects with opposite tilt meet. It is important to note that only a fraction of the anti-phase boundaries originate at the lattice steps on the substrate, which is otherwise typical for this type of defect. Here, an additional mechanism for anti-phase boundary formation an atomically flat surface of the substrate is illustrated in the inset of Fig. 12(b). While the group-V-sublattice of the substrate remains equally retained in the CuMnAs film, the tetragonal CuMnAs lattice may start either with the lower As-plane (As_1), or with the upper As-plane (As_2) rotated by 90°. This corresponds to a change in the stacking of the Mn and Cu layers in the individual grains. As a result, the c/2 lattice shift anti-phase boundaries form when islands with different stacking come into contact during further growth.

5 Correlation between defects and domain structure in CuMnAs

We have combined XMLD-PEEM antiferromagnetic (AF) domain imaging with microfocus scanning X-ray diffraction (SXRD) and low energy electron microscopy (LEEM) to elucidate the relationship between defect structures and magnetic order in 50nm thick CuMnAs films grown epitaxially on GaP. The as-grown films show two distinct domain types at room temperature, with the AF order parameter aligned with the CuMnAs [110] and [1-10] crystalline axes respectively. The typical domain size can vary from approximately 1 μm to up to tens of microns. In a free film, the domains tend to show a lamellar structure with a preferred directionality along the CuMnAs [110] and [1-10] crystalline directions. In patterned structures, where lateral edges are present, we find that the AF order parameter always aligns parallel to the edge. In addition, we observe characteristic lens-shaped domains with orthogonal spin axis growing from the edge.

The scanning X-ray diffraction measurements and LEEM measurements reveal that samples are honeycombed with pattern of bulk structural defect lines propagating along the CuMnAs [110]/ [1-10] crystalline axes. By comparison with the above STEM data we conclude that those correspond to inserted crystalline phase micro-twin defects in which the lattice is rotated with respect to the bulk [8]. The defect density is lowest in the samples that show the largest AF domains and the samples with the smallest domain structures exhibit the highest defect density. We find that the AF order parameter always aligns parallel to these crystal defects and thus imposes strict boundary conditions on the domain structure, similar to an edge which explains the variation of the average domain size in different areas.

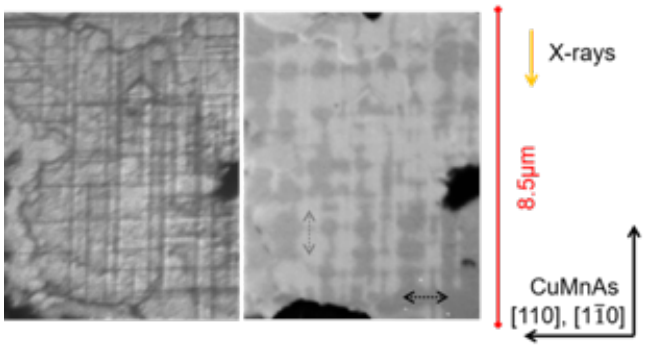

Figure 13: Correlation of the AF domain structure in a CuMnAs layer with structural line defects in a nonpatterned area. Left: LEEM image showing a dense, rectangular pattern of structural defect lines along the CuMnAs [110]/ [1-10] crystalline axes well as atomic step edges along different directions. Right: XMLD-PEEM image with the incident X-ray along the CuMnAs [110]. Light and dark areas correspond to spin axis orientations along the CuMnAs [110] and [1-10] crystalline axes respectively as indicated by the double-headed arrows. The black patches are dirt on the sample surface.

The impact of the defects on the domain configuration in a nonpatterned area is illustrated in Fig. 13 which compares the defect structure in a LEEM image with the AF domain configuration in the same area. The data are taken on one of the films with the highest defect density. Our data suggest that the lamellar domain structure in is largely due to the underlying defect structure.

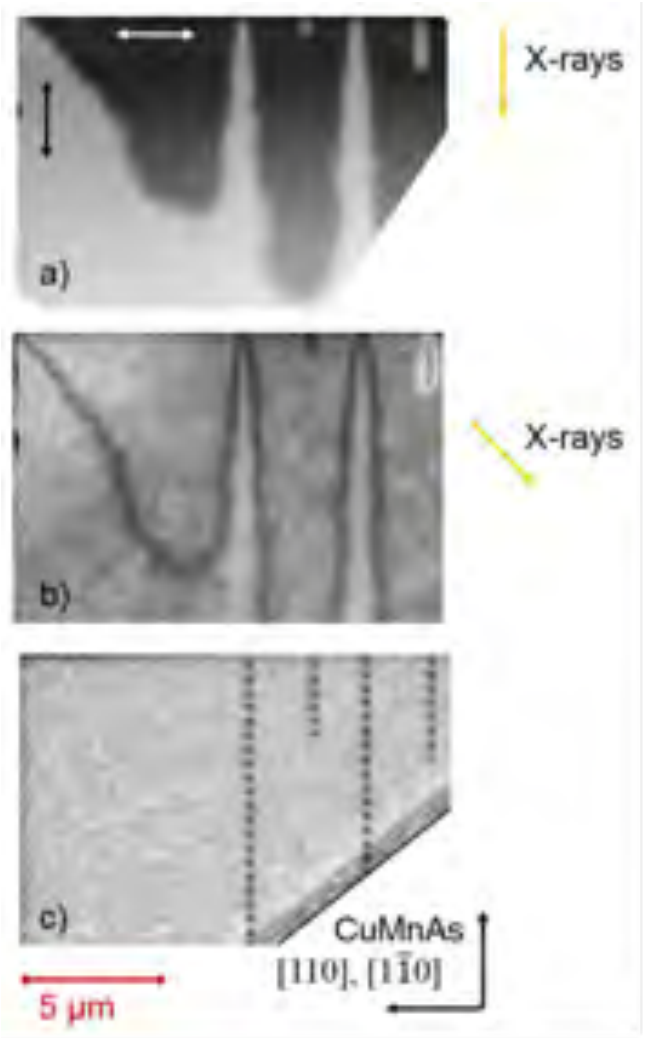

Figure 14: Correlation of the AF domain structure in a CuMnAs layer with structural line defects in nonpatterned area. a) X-PEEM image of a corner of a device with incident beam along CuMnAs [110] easy axis showing two distinct domain types. The double-headed arrows indicate the direction of the spin axis respectively. b) X-PEEM image with incident beam along [100] sensitive to the two different chiralities of the domain walls. c) Scanning XRD map of the same

Figure 14 shows a typical domain structure observed in a corner of a CuMnAs device fabricated from one of the layers with the lowest defect density. The image shows the parallel alignment of the order parameter along the edge and some characteristic lens-domains. By comparing the structure with scanning X-ray diffraction measurements of the same area, we find that those domains always coincide with a defect line running across its centre.

References

[1] Železný, J. *et al.* Relativistic néel-order fields induced by electrical current in antiferromagnets. *Physical Review Letters* **113**, 157201 (2014). 1410.8296.

[2] Wadley, P. *et al.* Electrical switching of an antiferromagnet. *Science* **351**, 587–590 (2016). 1503.03765.

[3] Železný, J., Wadley, P., Olejník, K., Hoffmann, A. & Ohno, H. Spin transport and spin torque in antiferromagnetic devices. *Nature Physics* **14**, 220–228 (2018).

[4] Wadley, P. *et al.* Current polarity-dependent manipulation of antiferromagnetic domains. *Nature Nanotechnology* **13**, 362–365 (2018). URL http://www.nature.com/articles/s41565-018-0079-1. arXiv:1711.05146.

[5] Kašpar, Z. *et al.* High resistive unipolar-electrical and fs-optical switching in a single-layer antiferromagnetic memory 1–22 (2019). URL http://arxiv.org/abs/1909.09071. 1909.09071.

[6] Wörnle, M. S. *et al.* Current-induced fragmentation of antiferromagnetic domains (2019). URL http://arxiv.org/abs/1912.05287. 1912.05287.

[7] Phillips, J. C. Axiomatic theories of ideal stretched exponential relaxation (SER). *Journal of Non-Crystalline Solids* **352**, 4490–4494 (2006).

[8] Krizek, F. *et al.* Molecular beam epitaxy of CuMnAs. *Physical Review Materials* **4**, 014409 (2020). URL https://link.aps.org/doi/10.1103/PhysRevMaterials.4.014409.

[9] Wang, M. *et al.* Spin flop and crystalline anisotropic magnetoresistance in CuMnAs. *Physical Review B* **101**, 094429 (2020). URL http://arxiv.org/abs/1911.12381https://link.aps.org/doi/10.1103/PhysRevB.101.094429. 1911.12381.

[10] Degen, C. L. Scanning magnetic field microscope with a diamond single-spin sensor. *Applied Physics Letters* **92**, 243111 (2008).

[11] Balasubramanian, G. *et al.* Nanoscale imaging magnetometry with diamond spins under ambient conditions. *Nature* **455**, 648–651 (2008).

[12] Wadley, P. *et al.* Antiferromagnetic structure in tetragonal CuMnAs thin films. *Scientific Reports* **5**, 17079 (2015).

[13] Grzybowski, M. J. *et al.* Imaging Current-Induced Switching of Antiferromagnetic Domains in CuMnAs. *Physical Review Letters* **118**, 057701 (2017). 1607.08478.